Electronic Supplementary Information for

Hot Carriers in Action: Multimodal Photocatalysis on Au@SnO_2 Core-Shell Nanoparticles

Xiaoqi Fu[*,†,‡] *Guangfang Grace Li,*[†] *Esteban Villarreal,*[†] *and Hui Wang*[*,†]

[†] *Department of Chemistry and Biochemistry, University of South Carolina, Columbia, South Carolina 29208, United States*

[‡] *School of Chemistry and Chemical Engineering, Jiangsu University, Zhenjiang, Jiangsu 212013, China*

[*] *To whom correspondence should be addressed.*

Email: wang344@mailbox.sc.edu (H. Wang); Phone: 1-803-777-2203; Fax: 1-803-777-9521.

xfu@ujs.edu.cn (X. Fu)

S1. Additional Experimental Details

S1.1 Chemicals and Materials

All chemical reagents were commercially available and used as received from the suppliers without further purification. Tetrachloroauric (III) acid trihydrate ($HAuCl_4 \cdot 3H_2O$, 99.99 %), sodium borohydride ($NaBH_4$, 99.99 %), and L-ascorbic acid (AA, 99.5 %) were purchased from Sigma-Aldrich. Cetyltrimethylammonium chloride (CTAC, > 96 %), sodium tin (IV) oxide trihydrate ($Na_2SnO_3 \cdot 3H_2O$, 98 %), rhodamine B (RhB), rhodamine 6G (R6G), basic blue 12 (BB12), and methylene blue (MB) were purchased from Alfa Aesar. Sodium hydroxide (NaOH) and ethanol (200 proof) were purchased from Fisher Scientific. Oxygen (99 %) and nitrogen (99 %) were purchased from Ratermann MFG Inc. Ultrapure water used for all experiments was distilled through a Thermo Barnstead Nanopure water purification system with a resistivity of 18.2 MΩ.

S1.2 Synthesis of Au Surface-Roughened Nanoparticles (SRNPs)

Au SRNPs were synthesized following a previous reported protocol involving kinetically controlled seed-mediated nanocrystal growth process.[1, 2] Colloidal Au seeds about 4 nm in size were first synthesized by reducing $HAuCl_4$ with $NaBH_4$ in the presence of CTAC as the surface-capping agent. Briefly, 0.3 mL of ice-cold, freshly prepared aqueous $NaBH_4$ (10 mM) was quickly injected into a solution containing CTAC (10.00 mL, 0.10 M) and $HAuCl_4$ (0.25 mL, 10 mM) under fast magnetic stir (1200 rpm). The reaction was allowed to proceed under magnetic stir for 1 min and then left undisturbed for 2 h. The seed solution was finally diluted 1000-fold with CTAC (0.10 M) solution for future use.

The nanocrystal growth solution was prepared by sequentially adding 0.5 mL of $HAuCl_4$ (10 mM) and 0.1 mL of AA (0.10 M) into 10 mL of CTAC (0.10 M) solution, followed by gentle mixing for 30 s. To initiate the growth of Au SRNPs, colloidal Au seeds were added into the growth solution. The reaction mixture was gently mixed for 30 s immediately and then left undisturbed for 4 h. The as-obtained Au SRNPs were centrifuged and washed with water through 3 centrifugation/redispersion cycles, and finally redispersed in 5.0 mL of water. The average diameters of the resulting Au SRNPs could be systematically tuned in the range of ~ 50 - 300 nm by varying the volumes of the colloidal Au seeds added. Decreasing the volumes of Au seeds resulted in increase of the overall sizes of the Au SRNPs.

S1.3 Synthesis of Au@SnO_2 Core-Shell Nanoparticles (CSNPs)

Au@SnO_2 CSNPs were synthesized by seed-mediated hydrolysis of Na_2SnO_3 [3, 4] using the Au SRNPs as the seeds. In a typical procedure, 1 mL of aqueous suspension of the as-synthesized Au SRNPs was diluted to 5 mL, and then 0.1 M NaOH was added to adjust the pH of the solution to 10. After the solution was heated to 80 °C in a water bath, 100 μL of Na_2SnO_3 (40 mM) was quickly injected under magnetic stir (250 rpm). The solution was stirred at 80 °C for another 2 h, and then allowed to cool to room temperature. The resulting Au@SnO_2 CSNPs were collected by centrifugation, then washed with water 3 times, and finally redispersed in water to form colloidal suspensions with particles concentration

of ~ 4.8 x 10^8 particles mL^{-1}. The particle concentration was estimated based on the amount of Au seeds used for the nanoparticle synthesis, as detailed in a previously published paper.[1] The average thickness of the SnO_2 shells could be systematically tuned by varying the volume of Na_2SnO_3 solution added while keeping the amount of colloid Au QSNP samples unchanged. Increasing the amount of Na_2SnO_3 resulted in thickening of the polycrystalline SnO_2 shells. Polycrystalline SnO_2 nanoshells with hollow interiors were obtained after exposing the Au@SnO_2 CSNPs to an aqueous solution containing 0.34 mM I_2 and 2.0 mM KI for 2 h,[5] through which the Au cores were selectively dissolved while keeping the SnO_2 shells intact.

S1.4 Characterizations of Nanoparticles

Transmission electron microscopy (TEM) images were obtained using a Hitachi H-8000 transmission electron microscope operated at an accelerating voltage of 200 kV. The atomic-level structures were resolved by high-resolution TEM (HRTEM) using a JEOL 2100F 200 kV FEGSTEM/TEM microscope. All samples for TEM measurements were drop-dried on 300 mesh Formvar/carbon coated Cu grids (Electron Microscopy Science Inc.). The size distributions of the nanoparticles were analyzed on the basis of TEM images containing more than 100 particles for each sample. The morphologies and compositions of the nanoparticle samples were also characterized by scanning electron microscopy (SEM) using a Zeiss Ultraplus thermal field emission scanning electron microscope. An energy dispersive spectroscopy (EDS) elemental analysis unit attached to the scanning electron microscope was used to quantify the Au and Sn stoichiometries in the samples and map the spatial distributions of Au and Sn elements. The Au/Sn atomic ratios were quantified based on the relative areas of the Au Mα and Sn Lα peaks in the EDS spectra. The samples for SEM and EDS measurements were dispersed in ethanol and drop-dried on silicon wafers. Powder X-ray diffraction (PXRD) patterns were record on a SAXSLab Ganesha at the South Carolina SAXS Collaborative (Cu $K\alpha$ = 1.5406 Å). The optical extinction spectra of colloidal nanoparticle samples were collected at room temperature using a Beckman coulter Du 640 spectrophotometer. The UV-visible diffuse reflectance spectroscopy (DRS) measurements were performed on a UV-2600 spectrophotometer (Shimadzu, Japan) equipped with an integration sphere using $BaSO_4$ powders as a reference.

S1.5 Calculation of Apparent Photonic Efficiency

The apparent photonic efficiency, η, of the hot carrier-driven photocatalytic degradation of RhB was defined as the ratio between the number of number of RhB molecules degraded (n_{RhB}) and the number of photons incident on the samples (n_{Photon}) during 1-hour reaction time. η can be expressed using the following equation:

$$\eta = \frac{n_{\mathrm{RhB}}}{n_{\mathrm{photon}}} \qquad \text{(Eqn. S1).}$$

n_{RhB} was calculated using the following equation:

$$n_{\mathrm{RhB}} = C_0 \times (I_{1h} / I_0) \times V \times N_A \qquad \text{(Eqn. S2),}$$

where C_0 is the initial concentration (Molarity) of RhB (4.2 x 10^{-6} M), I_0 is the absorbance at 553 nm before the reaction, I_{1h} is the absorbance at 553 nm after 1 h reaction time, V is the volume of solution (5.0 x 10^{-3} L), and N_A is the Avogadro's number, which is 6.022 x 10^{23}, respectively.

n_{Photon} was calculated based on the power density and wavelength of the incident laser using the following equation:

$$n_{\text{Photon}} = \frac{\rho_{\text{ex}} \times A \times \lambda_{ex}}{hc} \qquad \text{(Eqn. S3),}$$

where ρ_{ex} is the power density of the incident laser, A is the cross-section area of the laser illumination (0.16 cm^2 in our case), λ_{ex} is the laser excitation wavelength, c is the speed of light in air (3.0 x 10^8 m s^{-1}), and h is the Planck constant (6.626×10^{-34} m^2 kg s^{-1}), respectively.

Take the photodegradation of RhB catalyzed by the Au@SnO_2 CSNPs-ii under the excitation at 785 nm with a power density of 18.8 W cm^{-2} (1 W = 1 kg m^2 s^{-3}) as an example, I/I_0 was measured to be 0.408 at 1 h reaction time. Therefore,

$$n_{\text{RhB}} = 4.2\times10^{-6}\,\text{M} \times 5.0\times10^{-3}\,\text{L} \times 0.408 \times 6.022\times10^{23}\,\text{mole}^{-1} = 5.2\times10^{15},$$

and $$n_{\text{Photon}} = \frac{18.8\,\text{m}^2\,\text{kg}\,\text{s}^{-3}\,\text{cm}^{-2} \times 0.16\,\text{cm}^{-2} \times 785\times10^{-9}\,\text{m}}{6.626\times10^{-34}\,\text{m}^2\,\text{kg}\,\text{s}^{-1} \times 3.0\times10^{8}\,\text{m}\,\text{s}^{-1}} = 1.2\times10^{19}\,\text{s}^{-1} = 4.3\times10^{22}\,\text{h}^{-1}.$$

The value of η under this set of experimental conditions was calculated to be 1.2 x 10^{-7}. The values of η under other reaction conditions were calculated in the same way accordingly. The error bars associated with the η values shown in Figures 1H and 3B represented the standard deviations of the results of 3 experimental runs under each condition.

S2. Additional Figures

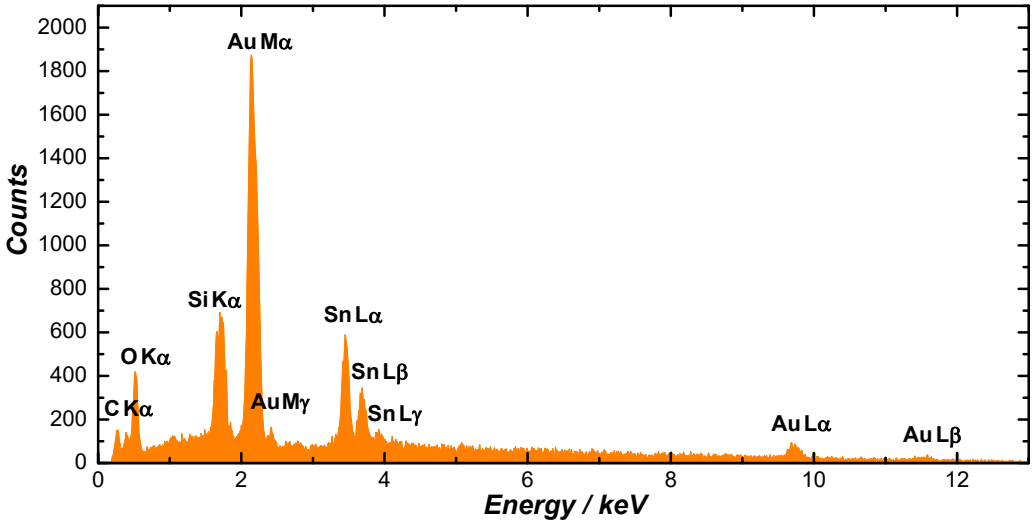

Figure S1. EDS spectrum of Au@SnO_2 CSNPs whose SEM image was shown in Figure 2B. The Si signals originated from the Si substrate used for SEM sample preparation. The Au Mα and Sn Lα peaks in the EDS spectrum were used for the quantification of the Au/Sn atomic ratios and the elemental mapping (see Figure 2C).

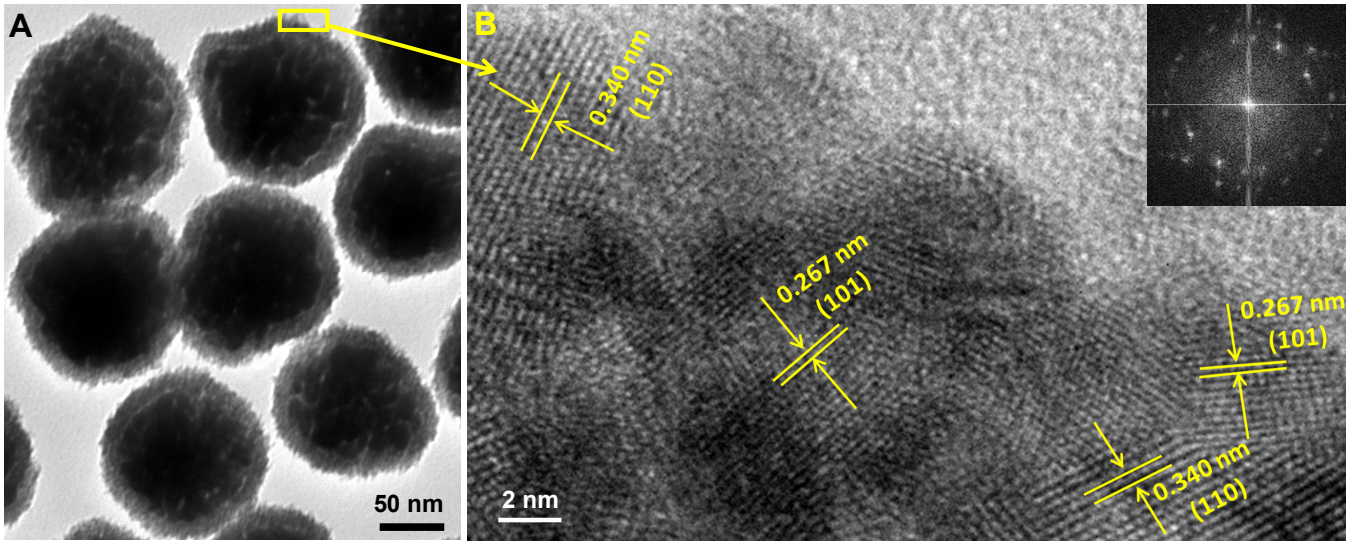

Figure S2. (A) HRTEM image of Au@SnO_2 CSNPs. (B) HRTEM image showing the atomic-level structural details of the polycrystalline SnO_2 shell in a local region enclosed by the yellow rectangle in panel A. The (110) and (101) lattice fringes of the tetragonal SnO_2 were well-resolved and the fast Fourier transform (FFT) image was shown in the inset panel at the up-right corner.

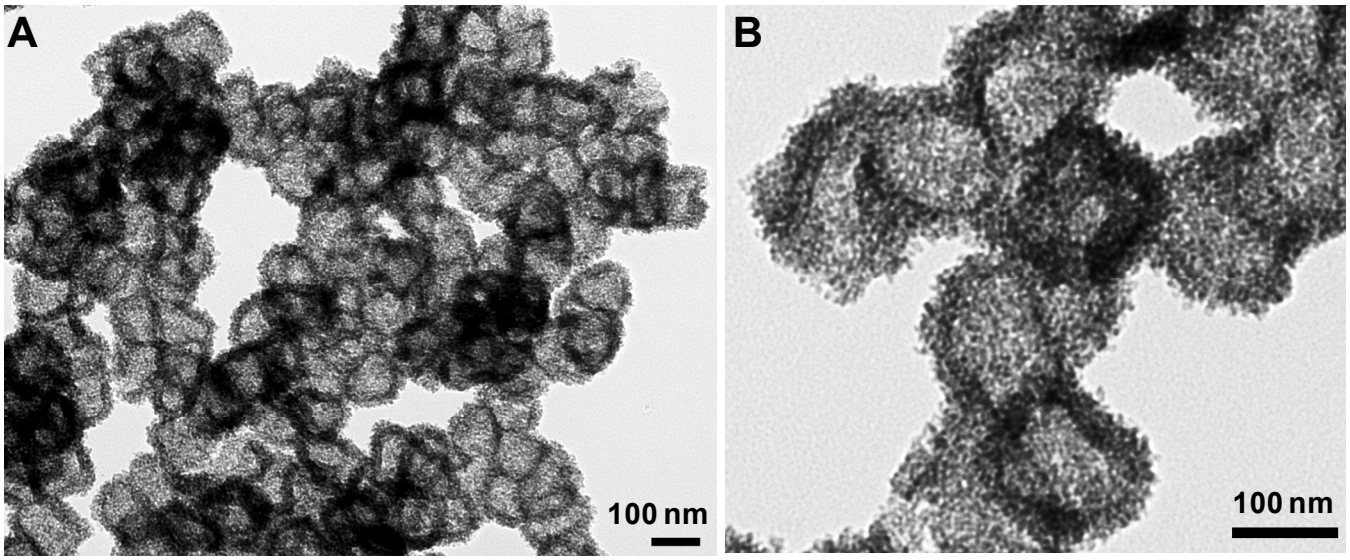

Figure S3. (A) TEM image of SnO_2 nanoshells that were obtained by selectively etching the Au cores of the Au@SnO_2 CSNPs in an aqueous solution containing 0.34 mM I_2 and 2.0 mM KI for 2 h. (B) Higher-magnification TEM image of the polycrystalline SnO_2 nanoshells.

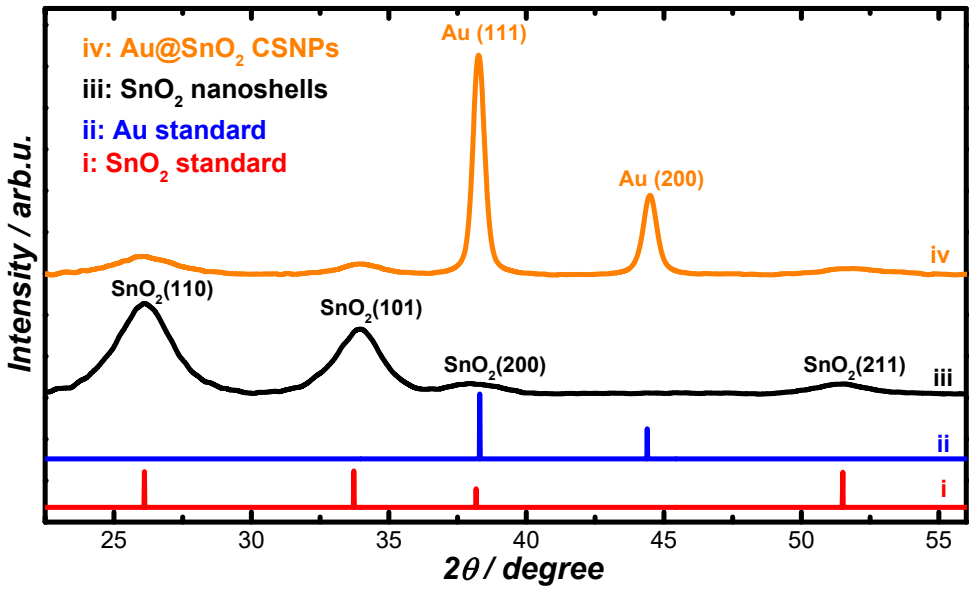

Figure S4. PXRD patterns of Au@SnO_2 CSNPs and SnO_2 nanoshells (obtained by etching the Au cores of the Au@SnO_2 CSNPs in KI/I_2 aqueous solution). The standard patterns of face-centered cubic (fcc) phase of Au (JCPDS no. 04-0784) and the tetragonal phase of SnO_2 (JCPDS no. 01-0625) were also shown for comparison. The diffraction patterns were offset for clarity.

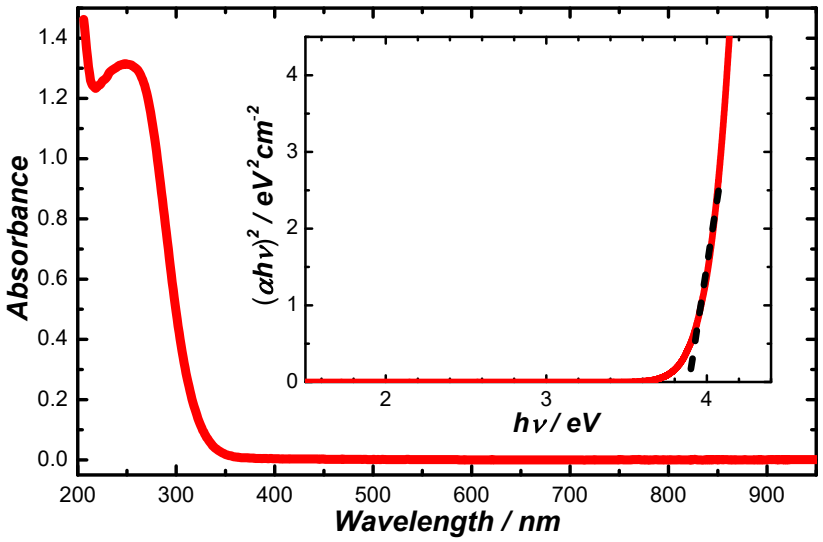

Figure S5. UV-Visible diffuse reflectance spectrum (DRS) of polycrystalline SnO_2 nanoshells. The inset shows the Tauc plots obtained from the DRS. The direct band gap of SnO_2 was determined to be 3.86 eV.

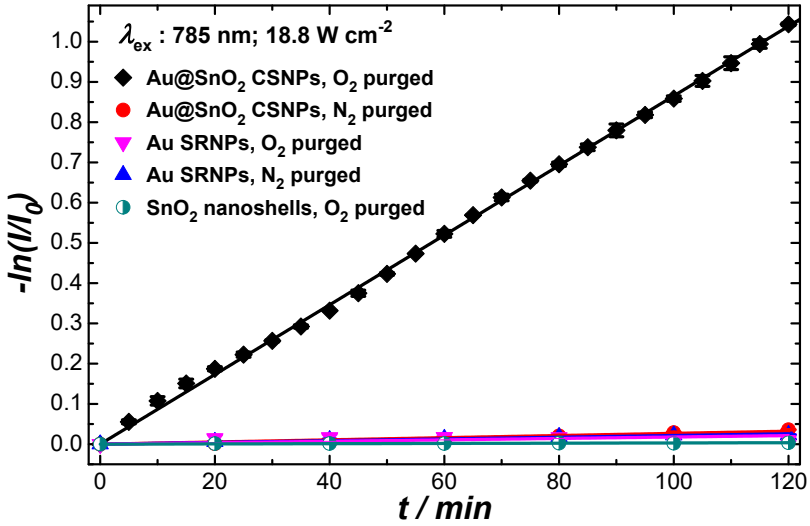

Figure S6. Temporal evolution of -ln(I/I_0) during photocatalytic degradation of RhB catalyzed by Au@SnO_2 CSNPs, Au SRNPs, and polycrystalline SnO_2 nanoshells in either O_2-pruged or N_2-purged solutions. The temporal evolution of the absorption peak intensity at 553 nm was monitored during the photocatalytic reactions under the illumination of 785 nm laser with an incident power density of 18.8 W cm^{-2}. The error bars represented the standard deviations obtained from 3 experimental runs. The solid lines showed the least squares curve fitting results.

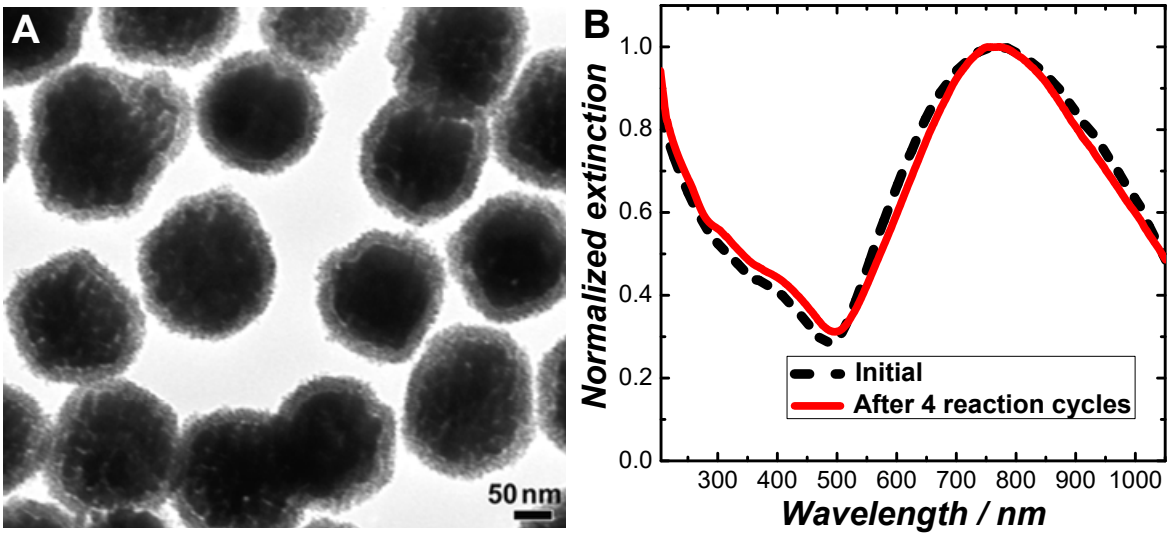

Figure S7. (A) TEM image of Au@SnO_2 CSNPs after 4 consecutive reaction cycles of photocatalytic degradation of RhB (see Figure 2E). (B) Optical extinction spectra of the as-synthesized Au@SnO_2 CSNPs and the Au@SnO_2 CSNPs recycled after 4 consecutive reaction cycles of photocatalytic degradation of RhB. In each photocatalytic reaction cycle, the reactant mixtures were exposed to 785 nm laser with an incident power density of 18.8 W cm^{-2} for 2 h.

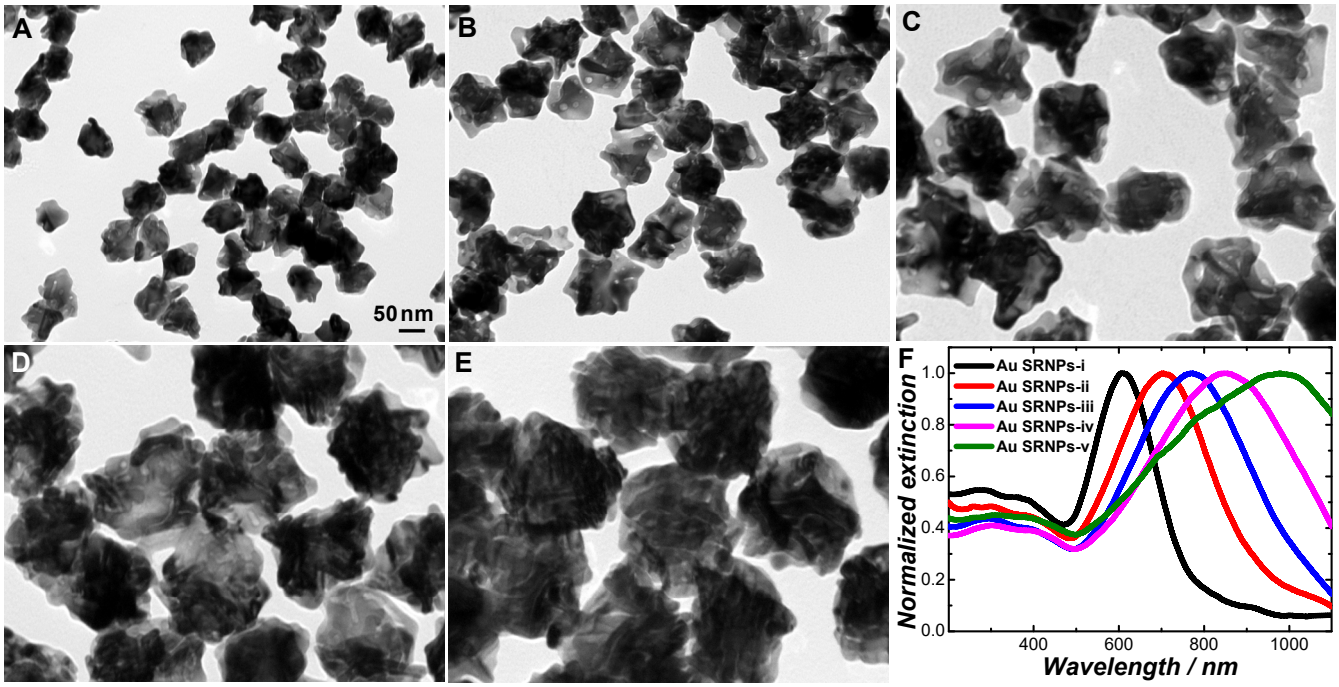

Figure S8. (A-E) TEM images of Au SRNPs of various average diameters: (A) Au SRNPs-i, 62 $\pm$ 4.6 nm; (B) Au SRNPs-ii, 96 $\pm$ 5.2 nm; (C) Au SRNPs-iii, 160 $\pm$ 7.3 nm; (D) Au SRNPs-iv: 197 $\pm$ 5.8 nm; (E) Au SRNPs-v: 226 $\pm$ 6.5 nm. All TEM images share the same scale bar in panel A. (F) Optical extinction spectra of Au SRNPs of various sizes. The extinction maxima were normalized to 1.

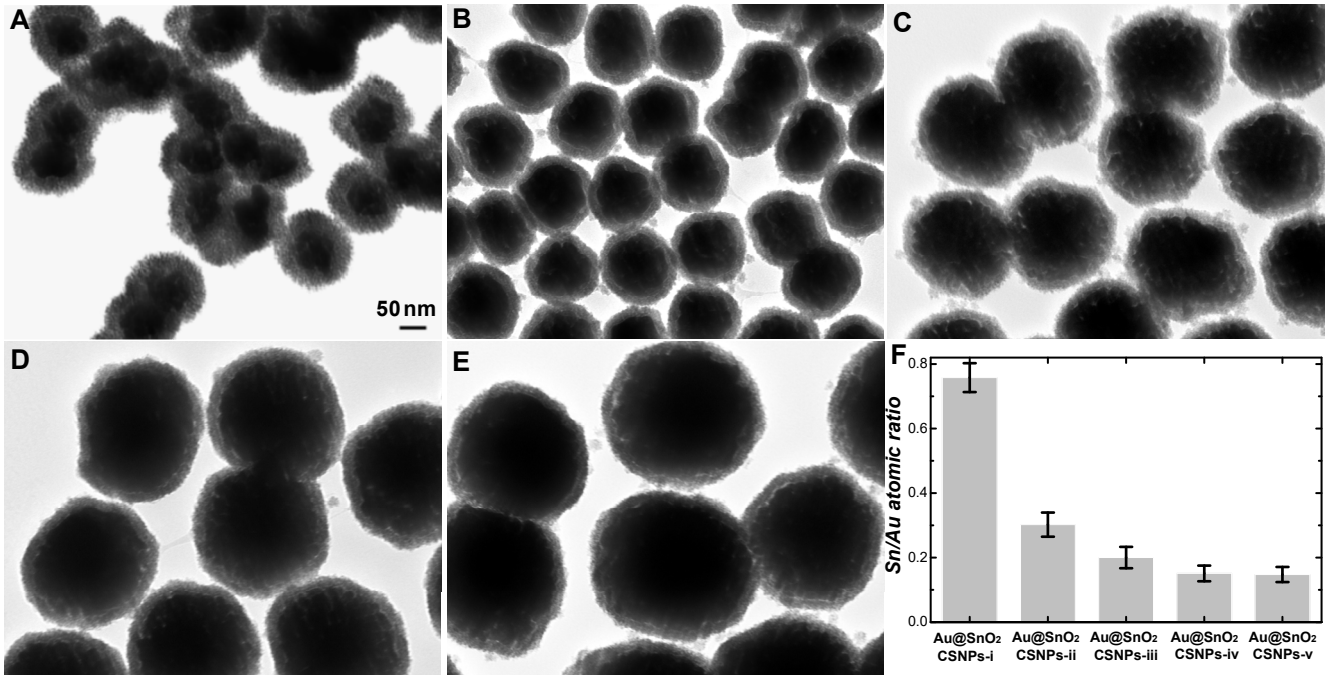

Figure S9. (A-E) TEM images of Au@SnO_2 CSNPs with nominally the same shell thickness around 17-22 nm and various core sizes. The overall particle diameters were: (A) CSNPs-i, 104 ± 6.4 nm; (B) CSNPs-ii, 130 ± 4.6 nm; (C) CSNPs-iii, 201 ± 4.8 nm; (D) CSNPs-iv, 237 ± 7.2 nm; (E) CSNPs-v, 271 ± 9.8 nm. All TEM images share the same scale bar in panel A. (F) Sn/Au atomic ratios of various Au@SnO_2 CSNPs quantified by EDS.

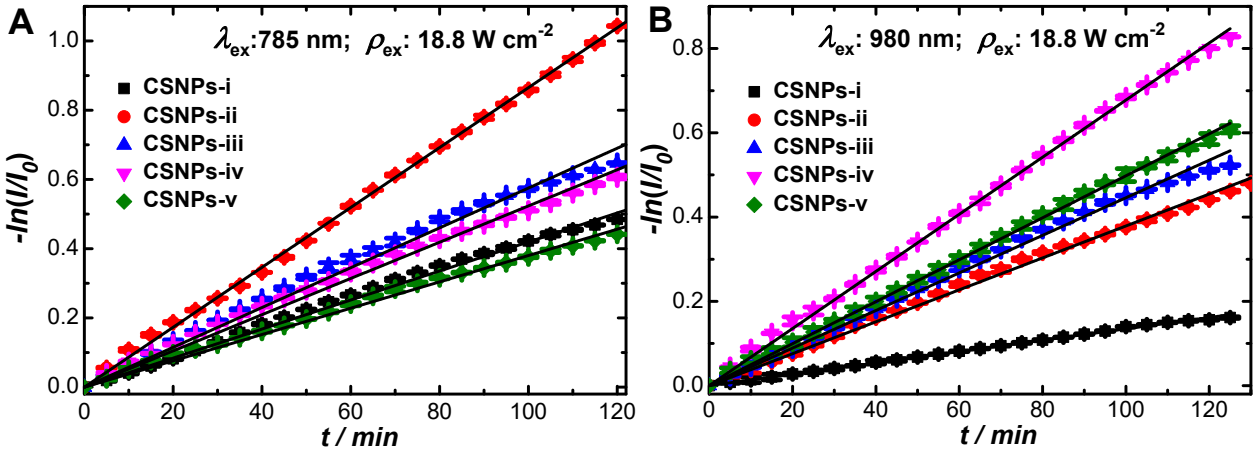

Figure S10. Temporal evolution of -ln(I/I_0) during the mineralization of RhB catalyzed by Au@SnO_2 CSNPs-i, CSNPs-ii, CSNPs-iii, CSNPs-iv, and CSNPs-v in O_2-pruged solutions under the illumination of (A) 785 nm and (B) 980 nm laser with an incident power density of 18.8 W cm^{-2}. The temporal evolution of the absorption peak intensity at 553 nm was monitored during the photocatalytic reactions. The error bars represented the standard deviations obtained from 3 experimental runs. The solid lines showed the least squares curve fitting results.

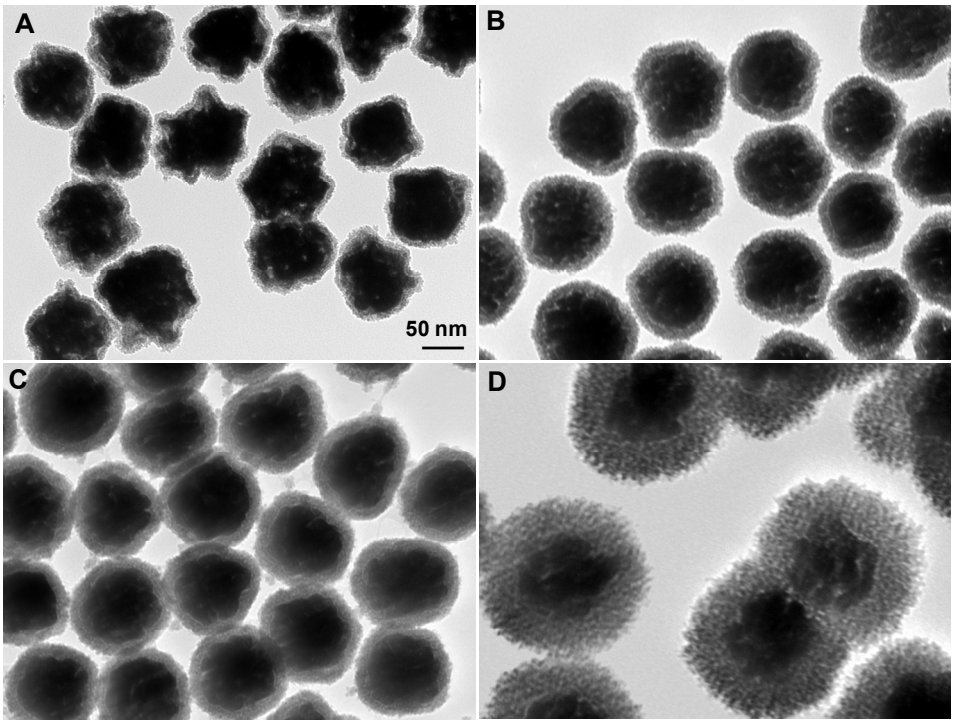

Figure S11. TEM images of Au@SnO_2 CSNPs with the same average Au core size (Au SRNPs-ii, 96 ± 5.2 nm in diameter) but different average SnO_2 shell thicknesses. The overall diameters of Au@SnO_2 CSNPs were (A) 106 ± 5.6, (B) 118 ± 4.8, (C) 130 ± 4.6, and (D) 182 ± 5.1 nm. As the thickness of SnO_2 shell increased, the plasmon resonance peak red-shifted. The samples shown in panels A-D were denoted as CSNPs-723, CSNPs-750, CSNPs-772, and CSNPs-830, respectively, according to their plasmon peak positions in the extinction spectra. All TEM images share the same scale bar in panel A.

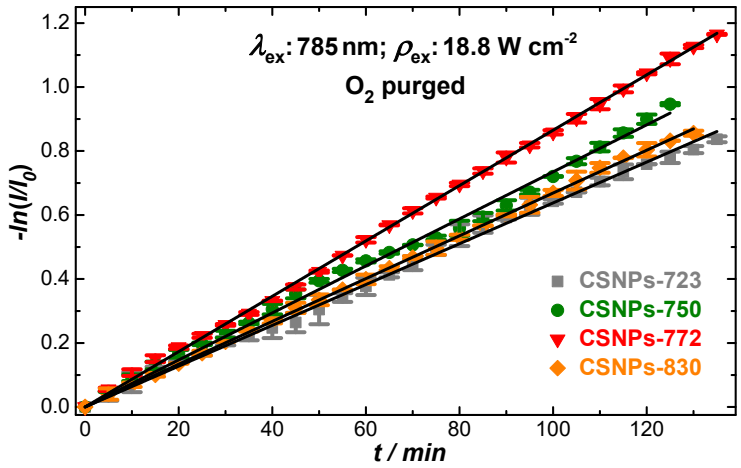

Figure S12. Temporal evolution of -ln(I/I_0) during the mineralization of RhB catalyzed by Au@SnO_2 CSNPs-723, CSNPs-750, CSNPs-772, and CSNPs-830 in O_2-pruged solutions. The temporal evolution of the absorption peak intensity at 553 nm was monitored during the photocatalytic reactions under the illumination of 785 nm laser with an incident power density of 18.8 W cm^{-2}. The error bars represented the standard deviations obtained from 3 experimental runs. The solid lines showed the least squares curve fitting results.

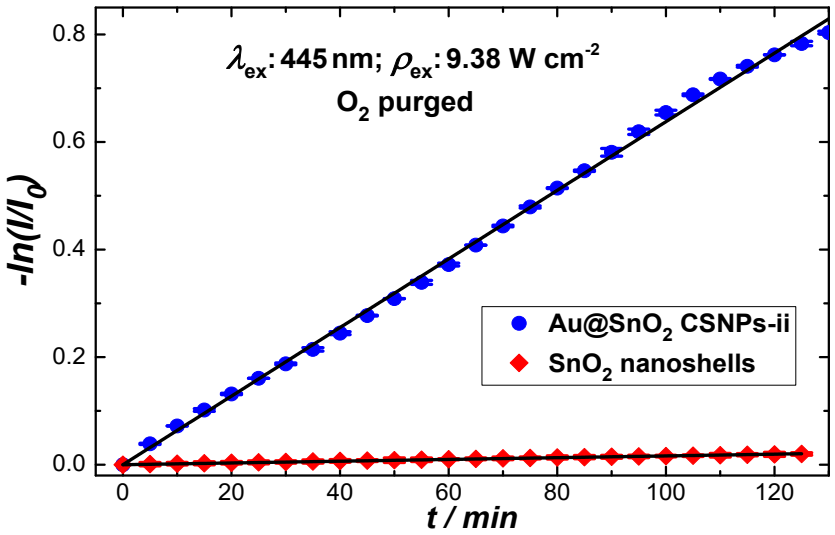

Figure S13. Temporal evolution of -ln(I/I_0) during the mineralization of RhB catalyzed by Au@SnO_2 CSNPs-ii and SnO_2 nanoshells (obtained by selectively etching the Au cores of the Au@SnO_2 CSNPs-ii in an aqueous solution containing 0.34 mM I_2 and 2.0 mM KI for 2 h) under the illumination of 445 nm laser with an incident power density of 9.38 W cm^{-2} in O_2-purged solutions. The error bars represented the standard deviations obtained from 3 experimental runs. The solid lines showed the least squares curve fitting results.

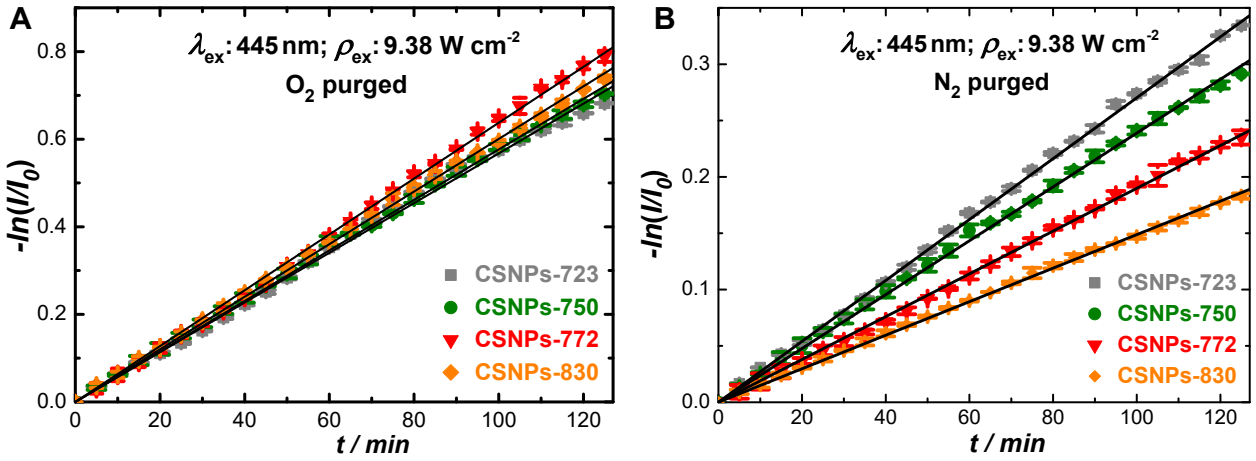

Figure S14. Temporal evolution of -ln(I/I_0) during the mineralization of RhB catalyzed by Au@SnO_2 CSNPs-723, CSNPs-750, CSNPs-772, and CSNPs-830 under the illumination of 445 nm laser with an incident power density of 18.8 W cm^{-2} in (A) O_2-purged and (B) N_2-purged solutions. The error bars represented the standard deviations obtained from 3 experimental runs. The solid lines showed the least squares curve fitting results.

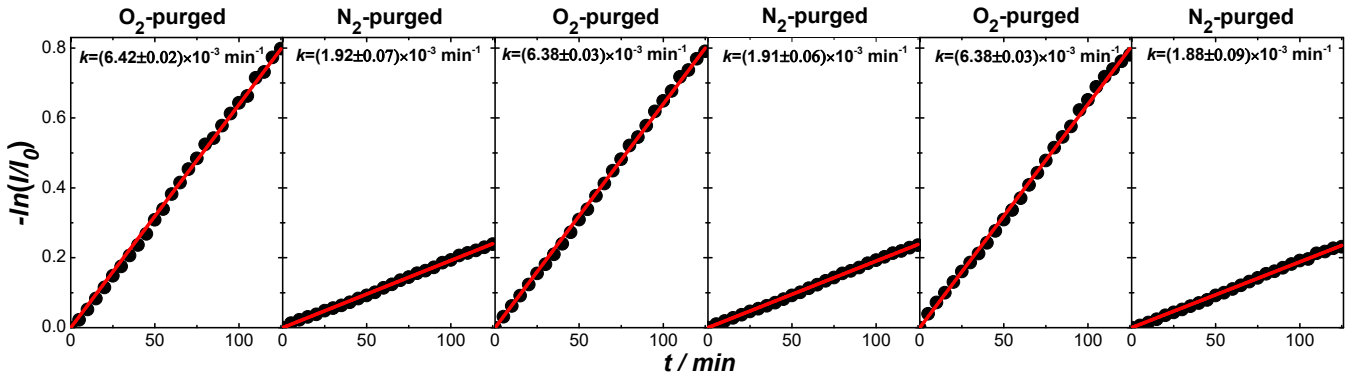

Figure S15. Temporal evolution of -ln(I/I_0) during the mineralization of RhB catalyzed by Au@SnO_2 CSNPs-ii under the illumination of 445 nm laser with an incident power density of 9.38 W cm^{-2} over 6 cycles of reactions. In cycles 1, 3, and 5, the photocatalytic reactions were carried out in O_2-purged solutions, while in cycles 2, 4, and 6, the reactions were carried out in N_2-purged solutions. The solid lines showed the least squares curve fitting results. The photocatalysts were recycled through centrifugation after each reaction cycle and then redispersed in 5 mL of RhB dye (4.2 μM) for the next reaction cycle. In each reaction cycle, the reaction progress was tracked by UV-visible absorption spectroscopy over a time period of 2 h with a time interval of 5 min for the measurements.

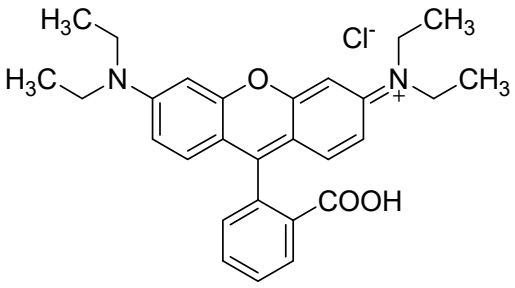

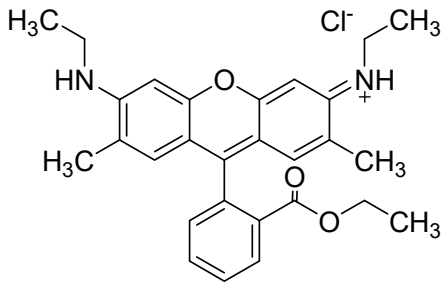

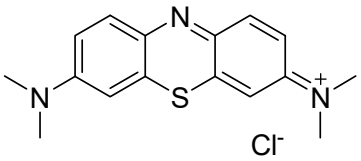

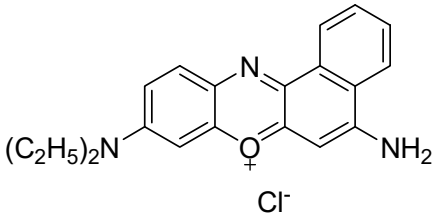

Figure S16. Molecular structures of RhB, R6G, MB, and BB12.

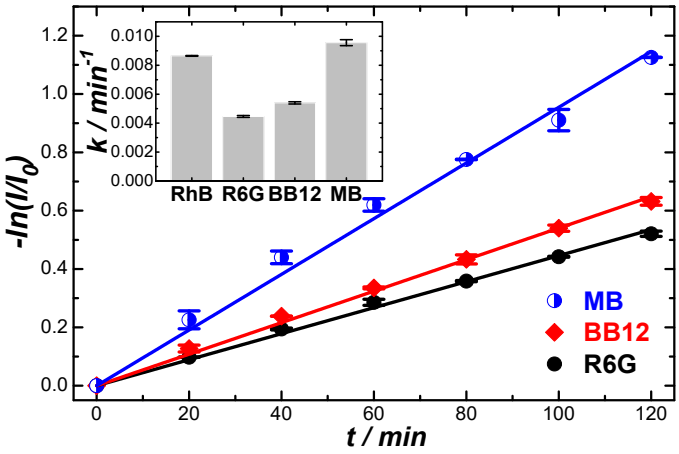

Figure S17. Temporal evolution of -ln(I/I_0) during the mineralization of R6G, MB, and BB12 catalyzed by Au@SnO_2 CSNPs-ii under the illumination of 785 nm laser at an incident power density of 18.8 W cm^{-2} in O_2-purged solutions. The error bars represented the standard deviations obtained from 3 experimental runs. The solid lines showed the least squares curve fitting results. The inset showed the comparison of the rate constant, k, for the photocatalytic degradation of RhB, R6G, BB12, and MB.

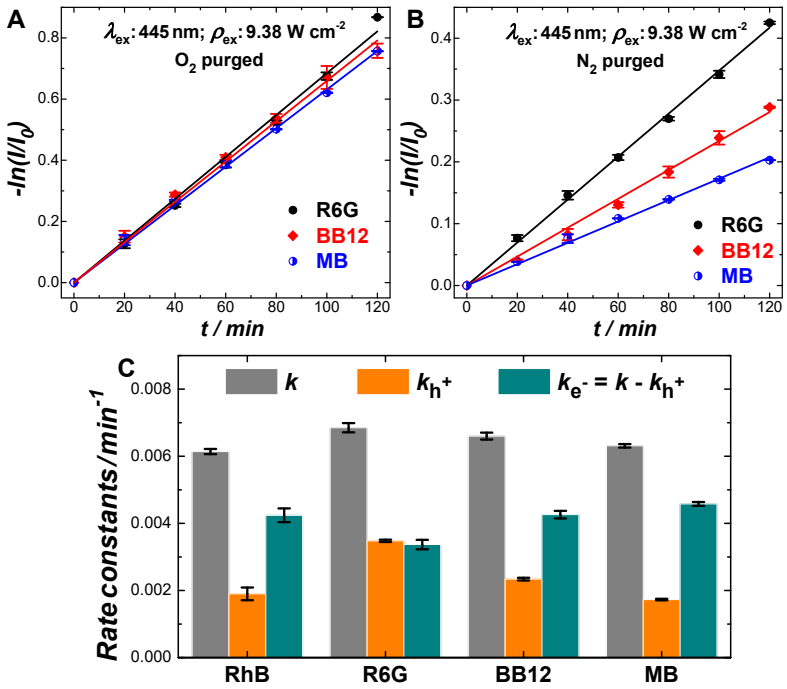

Figure S18. Temporal evolution of -ln(I/I_0) during the mineralization of R6G, MB, and BB12 catalyzed by Au@SnO_2 CSNPs-ii under the illumination of 445 nm laser with an incident power density of 9.38 W cm^{-2} in (A) O_2-purged and (B) N_2-purged solutions. The error bars represented the standard deviations obtained from 3 experimental runs. The solid lines showed the least squares curve fitting results. (C) Comparison of k, k_h^+, *and* k_e- for the photocatalytic degradation of RhB, R6G, BB12, and MB. The apparent rate constants, k, of the photocatalytic reactions driven by both electrons and holes were obtained from the results shown in panel A, while the rate constants of the hole-driven reactions, k_h^+, were obtained from the results shown in panel B. The rate constants of the electron-driven reactions, k_e-, were calculated by subtracting k_h^+ from k.

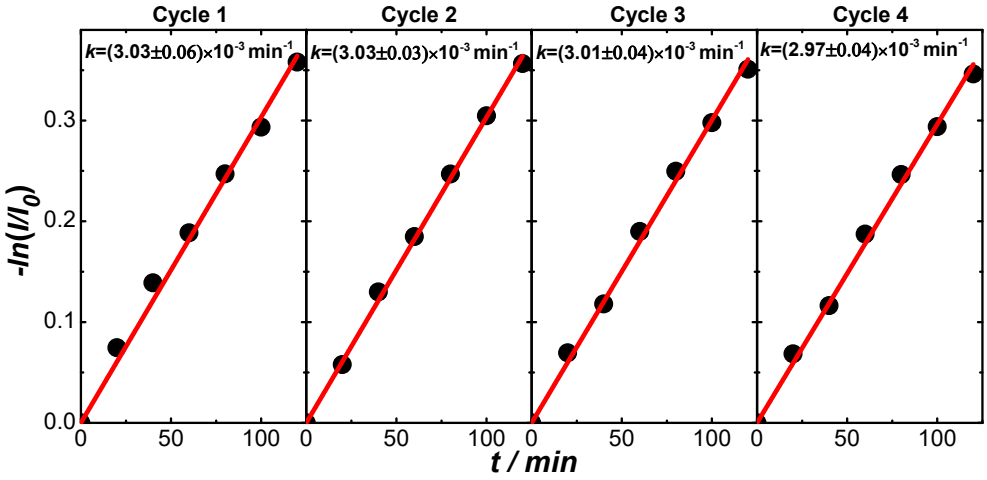

Figure S19. Catalytic durability of Au SRNPs-ii over 4 reaction cycles in N_2-purged RhB solutions under the illumination of 445 nm laser with an incident power density of 9.38 W cm^{-2}. The solid lines showed the least squares curve fitting results. The photocatalysts were recycled through centrifugation after each reaction cycle and then redispersed in 5 mL of RhB dye (4.2 μM) for the next reaction cycle. In each reaction cycle, the reaction progress was tracked by UV-visible absorption spectroscopy over a time period of 2 h with a time interval of 5 min for the measurements.

S3. References for Electronic Supplementary Information

1. Q. F. Zhang, D. A. Blom and H. Wang, *Chem. Mater*., 2014, **26**, 5131-5142.
2. Q. F. Zhang, N. Large, P. Nordlander and H. Wang, *J. Phys. Chem. Lett.*, 2014, **5**, 370-374.
3. G. Oldfield, T. Ung and P. Mulvaney, *Adv. Mater.*, 2000, **12**, 1519-1522.
4. S. H. Lee, I. Rusakova, D. M. Hoffman, A. J. Jacobson and T. R. Lee, *ACS Appl. Mater. Interfaces*, 2013, **5**, 2479-2484.
5. E. C. Cho, J. Xie, P. A. Wurm and Y. Xia, *Nano Lett.*, 2009, **9**, 1080-1084.